Solid State Communications 350 (2022) 114774

Contents lists available at ScienceDirect

Solid State Communications

journal homepage: www.elsevier.com/locate/ssc

Communication

Circularly-polarized-pulse-driven ultrafast optical currents in monolayer hexagonal Boron Nitride (*h*-BN)

Prabath Hewageegana [a,*], Vadym Apalkov [b]

[a] Department of Physics, University of Kelaniya, Kelaniya 11600, Sri Lanka
[b] Center for Nano-Optics (CeNO) and Department of Physics and Astronomy, Georgia State University, Atlanta, GA 30303, USA

ARTICLE INFO

Communicated by Xu Wen

Keywords:
Ultrafast optics
Hexagonal Boron Nitride
Topological resonance
Optical currents
Transferred charge

ABSTRACT

We predict the fundamentally fastest, ultrafast optical currents in monolayer hexagonal Boron Nitride (*h*-BN) by a circularly-polarized single-oscillation optical pulse. The femtosecond currents in gapped graphene and transition metal dichalcogenides have been discussed. However, the extension of the gapped graphene model for the large bandgap (~5 eV) has not been shown before. The strong optical pulse redistributes electrons between the bands and generates femtosecond currents during the pulse. The pulse generates both $x-$direction and $y-$direction currents due to charge transfer through the system. Thus, femtosecond ultrashort laser pulses provide an effective tool to manipulate and study the transport properties of electron systems and enhance the conductivity in solids at an ultrafast time scale with high temporal resolution. Ultrafast currents and charge transfer in monolayer *h*-BN may provide a fundamental basis for petahertz-band information processing.

1. Introduction

Femtosecond and attosecond-long ultrashort laser pulses provide an effective tool to manipulate and study the electron dynamics in solids at an ultrafast time scale with a high temporal resolution [1–16]. In particular, two dimensional (2D) materials exhibit unique properties due to the 2D nature of electron dynamics [17]. Among such 2D materials are dichalcogenides, complex oxides, bismuth telluride atomic quintuples, and boron nitride [18,19]. This new world of two-dimensional crystals is still very little researched, both in terms of their fundamental properties and their potential applications [20].

Two-dimensional monolayer hexagonal Boron Nitride (*h*-BN) possesses a direct bandgap of 4–6 eV at the Brillouin zone corner points, K, K' [21–23]. Similar to graphene, *h*-BN has a hexagonal lattice made of two sublattices, A and B (see Fig. 1(a)). Sublattices A and B consist of Boron and Nitride atoms and break the inversion ($\mathcal{P}$) symmetry and opens up gaps at the K, K'-points marking *h*-BN a wide-gap semiconductor [21] with D_{3h} point symmetry group [24,25]. However, the energy-dispersion symmetry between the K and K' valleys is protected by the time-reversal ($\mathcal{T}$) symmetry. Due to the broken inversion symmetry, the Berry curvature (topological magnetic field), $\boldsymbol{\Omega}$, has finite values with opposite signs in two valleys, K, and K', (see Fig. 1(b)). In contrast, the corresponding Berry curvature in graphene is non-zero only at the Dirac points, at which it has a δ-type singularity. The finite Berry curvature gives rise to a new effect, *topological resonance*, which occurs when the electron wave functions gradually accumulate the topological (geometric) phases along the electron Bloch trajectory in the field of the pulse [2–4,12,26]. In monolayer *h*-BN the corresponding Berry curvature is extended over finite regions near the K and K' points (see Fig. 1(b)). This allows electron wave functions, in monolayer *h*-BN, to gradually accumulate the topological phase.

Previously, we have shown that a single cycle of a circularly polarized optical pulse induces a large valley polarization, 25%–50%, in hexagonal Boron Nitride (*h*-BN) monolayers [27]. Such a strong pulse redistributes electrons between the bands and generates a valley-selective conduction band population. The mechanism of producing the fastest valley polarization fundamentally in *h*-BN monolayer has a topological origin [27]. Intense optical pulse contributes to the generation of strong nonlinear electric currents and finite electric charge transfer through the system. This is due to the strong coupling between the valence band (VB) and conduction band (CB) states. VB to CB transitions occur when an electron passes in the vicinity of the Dirac point (K or K') where the interband transition dipole matrix element (non-Abelian Berry connection) is enhanced [2–4].

The femtosecond currents, driven by a linearly-polarized single-oscillation of an intensive laser pulse in gapped graphene [15], and in transition metal dichalcogenides (TMDC) [28] have been discussed recently. However, the extension of the gapped graphene model for the bandgap of *h*-BN has not been shown before. Here, a large bandgap resembling the electronic structure of monolayer *h*-BN is introduced

* Corresponding author.
E-mail address: prabath@kln.ac.lk (P. Hewageegana).

https://doi.org/10.1016/j.ssc.2022.114774
Received 8 August 2021; Received in revised form 15 March 2022; Accepted 17 March 2022
Available online 18 April 2022

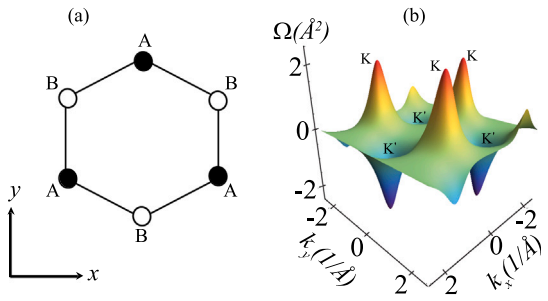

Fig. 1. (Color online) (a) The honeycomb lattice structure of graphene is made of two sublattices A (Boron) and B (Nitride). It is equivalent to assume that boron or nitrogen is on the A or on the B sublattice. (b) The Berry curvature (topological magnetic field), $\Omega(\mathbf{k}) = \frac{\partial}{\partial \mathbf{k}} \times \mathcal{A}(\mathbf{k})$, near the K and K' points in the extended zone picture. Here $\mathcal{A}$ is the intraband Berry connection.

contrary to other recent literature where mostly a small bandgap of gapped graphene and TMDC monolayers are investigated [15,28]. *h*-BN is of particular interest for the investigation of strong-field physics in two-dimensional materials, as energy dissipation to the material is generally reduced compared to small bandgap materials, which allows investigating more extreme regimes before optical breakdown.

In this article, we study the femtosecond currents driven by a circularly-polarized single-oscillation of an intensive laser pulse in monolayers of *h*-BN. A highly valley-specific electron population is allowed with helicity of the ultrafast circularly-polarized optical pumping [29–34]. We assume that the electron scattering (dephasing) in monolayer *h*-BN is longer than the duration of the optical pulse [35]. Then the corresponding electron dynamics in the field of the pulse is coherent and can, therefore, be described by the time-dependent Schrödinger equation (TDSE).

2. Model and main equations

The electron dynamics in the field of the optical pulse is described by the time-dependent Schrödinger equation (TDSE) with the Hamiltonian of the form

$$i\hbar \frac{d\Psi}{dt} = H_0\Psi - e\mathbf{F}(t)\mathbf{r}\Psi, \tag{1}$$

where $\mathbf{F}(t)$ is the electric field of the pulse, e is electron charge, and H_0 is the Hamiltonian of *h*-BN in the absence of the optical field. For *h*-BN, we consider the nearest neighbor tight-binding model, which is described by the following Hamiltonian [27]

$$H_0 = \begin{pmatrix} \frac{\Delta_g}{2} & \gamma f(\mathbf{k}) \\ \gamma f^*(\mathbf{k}) & -\frac{\Delta_g}{2} \end{pmatrix}. \tag{2}$$

Here $\Delta_g = E_B - E_N$ is the gap between the CB and the VB at the K or K' points and E_B and E_N are boron and nitrogen on-site energies. $f(\mathbf{k}) = \exp\left(i\frac{2\theta_1}{3}\right) + 2\exp\left(-i\frac{\theta_1}{3}\right)\cos\theta_2$, where $\theta_1 = \frac{\sqrt{3}ak_y}{2}$ and $\theta_2 = \frac{ak_x}{2}$. $\gamma = -2.33$ eV is the hopping integral, $a = 2.51$ Å is the lattice constant and $\mathbf{k} = (k_x, k_y)$ is the wave vector. The energies of CB and VB can be found from the above Hamiltonian, H_0 [27].

The applied electric field generates both the intraband and interband electron dynamics. The intraband dynamics is determined by the Bloch acceleration theorem [36]. Time-dependent wave vector $\mathbf{k}(\mathbf{q}, t)$, for an electron with initial wave vector $\mathbf{q}$, is expressed as

$$\mathbf{k}(\mathbf{q}, t) = \mathbf{q} + \frac{e}{\hbar}\int_{-\infty}^{t} \mathbf{F}(t')dt'. \tag{3}$$

Then, the solutions of Schrödinger equation (corresponding wave functions), within a single band α, i.e., without interband coupling, are the well-known Houston functions [37],

$$\Phi^{(\mathrm{H})}_{\alpha\mathbf{q}}(\mathbf{r}, t) = \Psi^{(\alpha)}_{\mathbf{k}(\mathbf{q},\mathbf{t})}(\mathbf{r}) \exp\left(i\sum_j \phi^{(\mathrm{j})}_{\alpha}(\mathbf{q}, t)\right), \tag{4}$$

where $\alpha = v, c$ for the VB and CB, correspondingly and $j = D$ and B respectively. $\phi^{(\mathrm{D})}_{\alpha}(\mathbf{q}, t) = \frac{-1}{\hbar}\int_{-\infty}^{t} dt' \left(E_{\alpha}[\mathbf{k}(\mathbf{q}, t')]\right)$ is the dynamic phase and $\phi^{(\mathrm{B})}_{\alpha}(\mathbf{q}, t) = \frac{e}{\hbar}\int_{-\infty}^{t} dt' \mathbf{F}\left(\mathcal{A}^{\alpha\alpha}[\mathbf{k}(\mathbf{q}, t')]\right)$ is the geometric (Berry) phase. $\Psi^{(\alpha)}_{\mathbf{k}}$ are Bloch-band eigenfunctions in the absence of the pulse field. Here $\mathcal{A}^{\alpha\alpha} = \left\langle \Psi^{(\alpha)}_{\mathbf{q}} | i\frac{\partial}{\partial \mathbf{q}} | \Psi^{(\alpha)}_{\mathbf{q}} \right\rangle$ is the intraband Berry connection. The expressions for the intraband Berry connections, $\mathcal{A}^{\alpha\alpha} = (\mathcal{A}^{\alpha\alpha}_x, \mathcal{A}^{\alpha\alpha}_y)$, can be found from the tight-binding Hamiltonian [27].

The interband electron dynamics is described by TDSE (1). The solution of TDSE can be expanded in the basis of Houston functions $\Phi^{(H)}_{\alpha\mathbf{q}}(\mathbf{r}, t)$ [38],

$$\Psi_{\mathbf{q}}(\mathbf{r}, t) = \sum_{\alpha=c,v} \beta_{\alpha\mathbf{q}}(t)\Phi^{(H)}_{\alpha\mathbf{q}}(\mathbf{r}, t), \tag{5}$$

where $\beta_{\alpha\mathbf{q}}(t)$ are expansion coefficients, which satisfies the following system of coupled differential equations

$$i\hbar\frac{\partial B_{\mathbf{q}}(t)}{\partial t} = -e\mathbf{F}(t)\hat{\mathcal{A}}(\mathbf{q}, t)B_{\mathbf{q}}(t)\ , \tag{6}$$

where the wave function (vector of state) $B_q(t)$ and $\hat{\mathcal{A}}(\mathbf{q}, t)$ are defined as

$$B_{\mathbf{q}}(t) = \begin{bmatrix} \beta_{c\mathbf{q}}(t) \\ \beta_{v\mathbf{q}}(t) \end{bmatrix} \text{ and } \hat{\mathcal{A}}(\mathbf{q}, t) = \begin{bmatrix} 0 & \mathcal{D}^{cv}(\mathbf{q}, t) \\ \mathcal{D}^{vc}(\mathbf{q}, t) & 0 \end{bmatrix} \tag{7}$$

$$\text{where } \mathcal{D}^{cv}(\mathbf{q}, t) = \mathcal{A}^{cv}[\mathbf{k}(\mathbf{q}, t)] \times \exp\left(i\sum_j \phi^{(\mathrm{j})}_{cv}(\mathbf{q}, t)\right), \tag{8}$$

$$\phi^{(\mathrm{j})}_{cv}(\mathbf{q}, t) = \phi^{(\mathrm{j})}_{v}(\mathbf{q}, t) - \phi^{(\mathrm{j})}_{c}(\mathbf{q}, t) \tag{9}$$

$$\mathcal{A}^{cv}(\mathbf{q}) = \left\langle \Psi^{(c)}_{\mathbf{q}} | i\frac{\partial}{\partial \mathbf{q}} | \Psi^{(v)}_{\mathbf{q}} \right\rangle. \tag{10}$$

Here $\mathcal{A}^{cv}(\mathbf{q})$ is a matrix element of the non-Abelian Berry connection [27,39–41].

During the pulse, both intraband and interband electron dynamics generate electric current, $\mathbf{J}(t) = \{J_x(t), J_y(t)\}$. The current has both interband and intraband contributions, $\mathbf{J}(t) = \mathbf{J}^{(\mathrm{intra})}(t) + \mathbf{J}^{(\mathrm{inter})}(t)$, where the intraband current is proportional to the group velocity and has the following form

$$\mathbf{J}^{(\mathrm{intra})}(t) = \frac{eg_s}{a^2}\sum_{\alpha=\mathrm{c,v},\mathbf{q}} \left|\beta_{\alpha}(\mathbf{q}, t)\right|^2 \mathbf{v}^{(\alpha)}(\mathbf{k}(\mathbf{q}, t))\ , \tag{11}$$

where $\mathbf{v}^{(\alpha)}_{\mathbf{k}} = \frac{\partial}{\partial \mathbf{k}}E^{(\alpha)}(\mathbf{k})$ is the group velocity and $g_s = 2$ is spin degeneracy. The group velocities can be written as

$$V^{\mathrm{c}}_x(\mathbf{k}) = -V^{\mathrm{v}}_x(\mathbf{k}) = \eta \times \sin\theta_2\left(\cos\theta_1 + 2\cos\theta_2\right) \tag{12}$$

$$V^{\mathrm{c}}_y(\mathbf{k}) = -V^{\mathrm{v}}_y(\mathbf{k}) = \sqrt{3}\eta \times \sin\theta_1\cos\theta_2. \tag{13}$$

Where $\eta = \frac{-a\gamma^2}{\hbar\sqrt{|\gamma f(\mathbf{k})|^2 + \frac{\Delta_g^2}{4}}}$.

The interband current is given by the following expression

$$\begin{aligned}\mathbf{J}^{(\mathrm{inter})}(t) = i\frac{eg_s}{\hbar a^2}\sum_{\substack{\mathbf{q} \\ \alpha,\alpha'=\mathrm{v,c} \\ \alpha\neq\alpha'}} & \beta^*_{\alpha'}(\mathbf{q}, t)\beta_{\alpha}(\mathbf{q}, t) \\ & \times \exp\{i\sum_j \phi^{(\mathrm{j})}_{\alpha'\alpha}(\mathbf{q}, t)\} \\ & \times \left[E_{\alpha'}(\mathbf{k}(\mathbf{q}, t)) - E_{\alpha}(\mathbf{k}(\mathbf{q}, t))\right]\mathcal{A}^{(\alpha\alpha')}(\mathbf{k}(\mathbf{q}, t))\,,\end{aligned} \tag{14}$$

where

$$\phi^{(\mathrm{j})}_{\alpha'\alpha}(\mathbf{q}, t) = \phi^{(\mathrm{j})}_{\alpha}(\mathbf{q}, t) - \phi^{(\mathrm{j})}_{\alpha'}(\mathbf{q}, t), \tag{15}$$

3. Results and discussion

We consider a single-oscillation ultrafast circularly-polarized pulse propagating along the z axis. The electric field $\mathbf{F}(t)$ is given by the following expression

$$F_x(t) = F_0\left[1 - 2\left(\frac{t}{\tau}\right)^2\right]e^{-(t/\tau)^2},\ F_y(t) = \pm 2\left(\frac{t}{\tau}\right)F_0 e^{-(t/\tau)^2}, \tag{16}$$

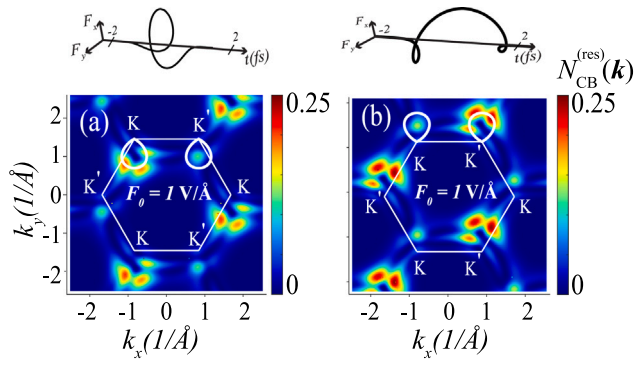

Fig. 2. (Color online) Residual CB population $N_{\rm CB}^{\rm (res)}(\mathbf{k})$ for h-BN in the extended zone picture. (a) For right circular polarization with the amplitude of 1 V Å^{-1} (b) Same as in (a) but for the left circular polarization. Inset [left (RCP) and right (LCP)]: Waveform of the pulse $\mathbf{F}(t) = \{F_x(t), F_y(t)\}$ as a function of time t. The straight and cove white lines represent the boundary of the first Brillouin zone, with the K, K'-points, and the separatrix respectively. $\Delta_g = 5$ eV and $\tau = 0.5$ fs.

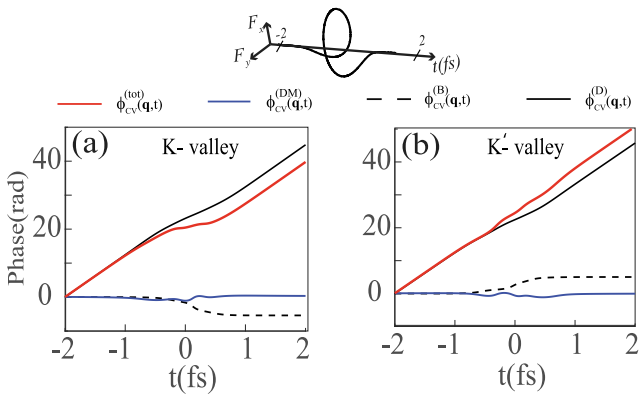

Fig. 3. (Color online) For a pulse with $\tau = 0.5$ fs right-hand circular polarization and amplitude $F_0 = 1$ V Å^{-1}, phases $\phi_{cv}^{(tot)}(\mathbf{q},t)$, $\phi_{cv}^{(D)}(\mathbf{q},t)$, $\phi_{cv}^{(B)}(\mathbf{q},t)$, and $\phi_{cv}^{(DM)}(\mathbf{q},t)$ are shown for different valleys. (a) For the K valley. (b) For the K' valley.

where τ determines the pulse duration and its mean frequency. The $\pm$ sign in Eq. (16) defines helicity of the applied pulse: + for the right-handed circular polarization (RCP) and – for the left-handed circular polarization (LCP). Defined by Eq. (16), these left- and right-handed pulses are $\mathcal{T}$-reversed with respect to one another.

The excursion of electron crystal momentum during the pulse can be estimated as

$$\Delta k \sim \frac{\pi e F_0}{\hbar\bar{\omega}}, \tag{17}$$

where e is unit charge and $\hbar$ is the reduced Planck's constant. An ultrafast pulse has no definite frequency since its Fourier component is widely distributed in the frequency space. One can calculate the $\bar{\omega}$ of such an optical pulse as,

$$\bar{\omega} = \int \omega S(\omega) d\omega / \int S(\omega) d\omega, \tag{18}$$

where the pulse spectrum, $S(\omega)$ is defined as $S(\omega) = |\int \mathbf{F}(t) e^{i\omega t} d\omega|^2$. For the pulse, described in Eq. (16) with $\tau = 0.5$ fs, we have calculated $\hbar\bar{\omega} = 2.4$ eV. To travel half of the Brillouin zone, this excursion should be $\Delta k \sim \pi/a$, where a is the lattice constant of monolayer h-BN. Taking $\hbar\bar{\omega} = 2.4$ eV and $a = 2.51$ Å, we obtain $F_0 \approx \hbar\bar{\omega}/(ea) \approx 1$ V/Å. Estimating from Eq. (17), we obtain $\Delta k \approx 0.2$ Å^{-1}. These values are in qualitative agreement with the calculation results illustrated in Fig. 2.

Below we consider pulses of moderately high field amplitudes, $F_0 \sim 1$ V/Å. At such intensities, the number of photons per pulse within the minimum coherence area of $\sim \lambda^2$, where $\lambda \sim 1$ μm is the wavelength, $N_p \sim \frac{c\tau\lambda^2 F_0^2}{4\pi\hbar\bar{\omega}} \sim 10^9$, where c is the speed of light; we assume realistic parameters: $\tau \sim 0.5$ fs is the pulse duration, and $\hbar\bar{\omega} \sim 2.4$ eV is the mean photon energy. With a large photon number involved, it is legitimate to describe $\mathbf{F}(t)$ as a classical electric field keeping quantum-mechanical description of the solid. This is a usual approach in high-field optics [42–44]. Below, we numerically solve the corresponding Schrödinger equation in the truncated Houston basis without further approximations.

Fig. 2 shows the residual CB population distribution in the reciprocal space in h-BN for $F_0 = 1$ V Å^{-1} and $\tau = 0.5$ fs. The excitation pulse has right-handed circular polarization [in Fig. 2(a)] and left-handed circular polarization [in Fig. 2(b)]. The valley selectivity is significantly high: the right-handed pulse populates predominantly the K valleys [see Fig. 2(a)], while the left-handed pulse mostly the K′ valleys [see Fig. 2(b)]. Such a difference in the populations of the K vs. K′ valleys are referred to as valley polarization which is protected by the $\mathcal{T}$-symmetry [27]. The K-valley population for a given handedness pulse is inverted ($\mathbf{k} \leftrightarrow -\mathbf{k}$) to the K′-valley population for the opposite handedness (compare the corresponding panels in Fig. 2. For a given valley, its population predominantly occurs along a closed curve whose apexes are at the K and K′ points (called the separatrix [45]).

The origin of such valley-selective CB population is the topological resonance due to the accumulation of topological (geometric) phases along the electron Bloch trajectory in the field of the pulse. The topological phase is a combination of the $\phi_{cv}^{(B)}(\mathbf{q},t)$ and the phase of the dipole matrix element, $\phi_{cv}^{(DM)}(\mathbf{q},t)$. The topological resonance occurs when the time variation of the topological phase cancels the time variation of the dynamic phase or in other words when the total phase $\phi_{cv}^{(tot)}(\mathbf{q},t)$ is stationary. The corresponding phases, $\phi_{cv}^{(tot)}(\mathbf{q},t)$, $\phi_{cv}^{(D)}(\mathbf{q},t)$, $\phi_{cv}^{(B)}(\mathbf{q},t)$, and $\phi_{cv}^{(DM)}(\mathbf{q},t)$, are shown in Fig. 3 for monolayer h-BN.

We can clearly see that the phases $\phi_{cv}^{(B)}(\mathbf{q},t)$ and $\phi_{cv}^{(DM)}(\mathbf{q},t)$, for a given valley, have opposite signs [see Fig. 3(a) and (b)]. Thus, the time variation of $\phi_{cv}^{(tot)}(\mathbf{q},t)$ strongly depends on the valley, K or K'. As we see in the case of Fig. 3, the total phase, $\phi_{cv}^{(tot)}(\mathbf{q},t)$, is stationary at $t = 0$ only for the K-valley [Fig. 3(a)] but not for the K'-valley [Fig. 3(b)]. Thus, for the right-hand circularly-polarized pulse, the topological resonance favors the residual population of the K-valley while the residual CB population of the K'-valley is relatively small. In contrast, for the left-hand circularly-polarized pulse, the topological phase for a given valley has the opposite sign. Consequently, it is the K' valley that is predominantly populated, and K-valley is almost unpopulated, i.e., the valley polarization is exactly the opposite.

Due to the residual conduction band population, ultrafast field-driven intraband and interband electron dynamics generate an electric current. For the circularly polarized pulse, the longitudinal current J_x, i.e., the current in the x- direction, and the transverse current J_y, i.e., the current in the y- direction, are generated. The generated electric currents are shown in Fig. 4 for different values of the pulse duration, τ. As one can see, the magnitude of the x-direction and y-direction currents decrease with the τ, as shown in Fig. 4. This behavior is because the duration of the pulse determines the energy of the pulse. Both x and y components of the currents show the same profile during the pulse, i.e., two fs $< t <$ 2 fs, but after the pulse, J_x and J_y have oscillatory behavior with the frequency of oscillations that depends on the bandgap of monolayer h-BN. Such oscillations in the residual current are because the main contribution to the current is the interband one, while the intraband contribution, which depends only on conduction and valence bands population and thus does not show significant oscillation after the pulse.

The intraband current is completely determined by the asymmetry of the electron density distributions in the CB and VB. The x-direction current, which is a combination of both interband and intraband contributions, is shown in Fig. 4(a). Unlike in small band gap 2D material like gaped graphene, the CB population distribution is asymmetric with

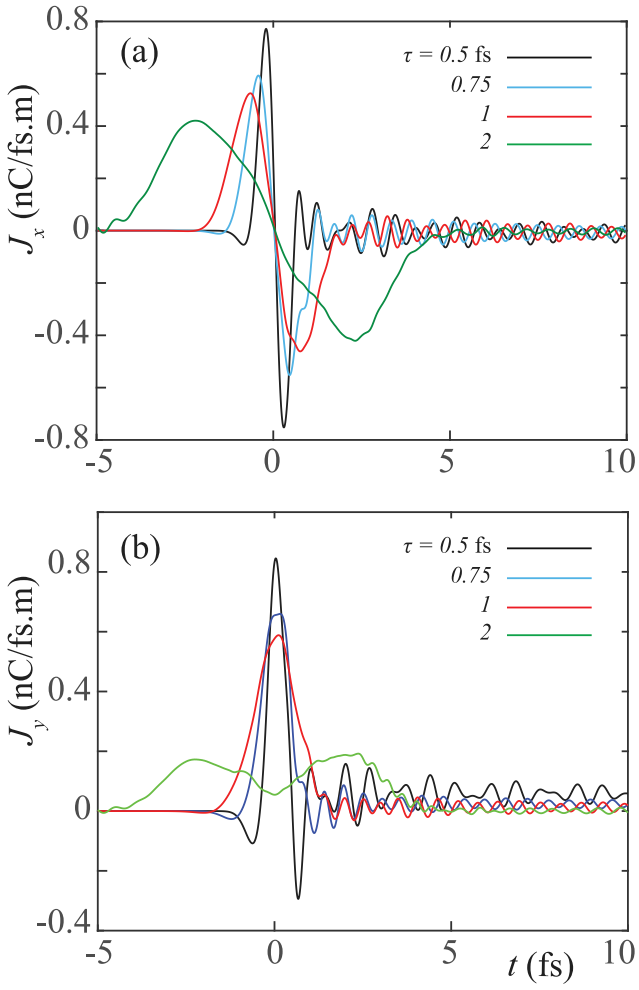

Fig. 4. (Color online) The current densities in monolayer h-BN are shown as a function of time for various pulse durations, 0.5 fs, 0.75 fs and 1 fs. (a) The current density, J_x is shown along the direction of the maximum field. (b) Same as in (a), but for the direction, y, normal to the maximum field. The applied pulse has right circular polarization with $F_0 = 0.5$ V/Å. The band gap of h-BN is 5 eV.

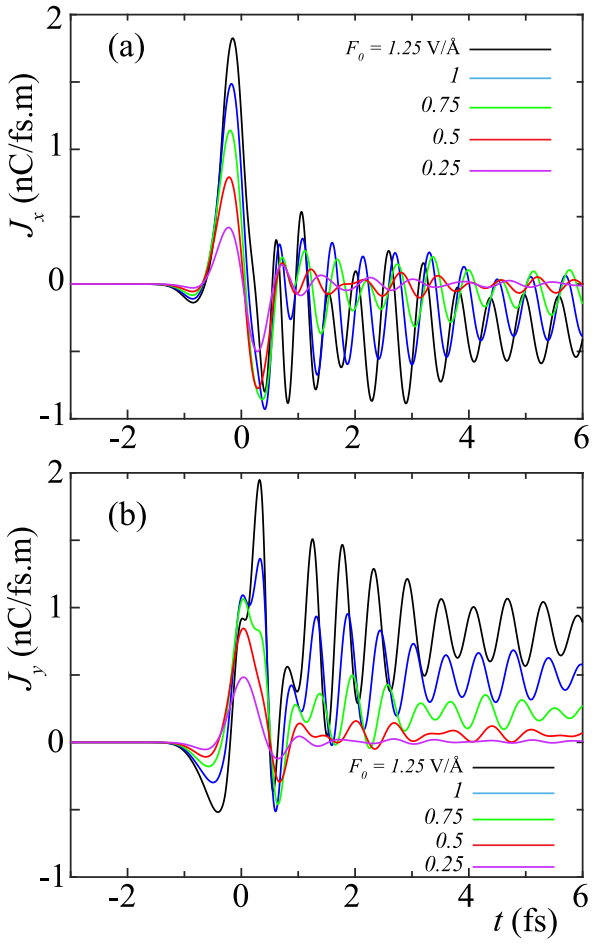

Fig. 5. (Color online) Same as in Fig. 4, for various field's amplitudes, F_0, 1 VÅ^{-1}, 0.75 V Å^{-1}, 0.5 V Å^{-1} and 0.25 V Å^{-1}. The applied pulse has right circular polarization with $\tau = 0.5$ fs.

respect to the y-axis both during and after the pulse. Thus, the y-direction current J_y for h-BN is also determined by both interband and intraband contributions [see Fig. 4(b)]. The x-direction current as a function of time is oscillating with the frequency that depends on the bandgap, see Fig. 4(a) while the y-direction current is almost unidirectional, see Fig. 4(b)]. These oscillations are a mixture of oscillating interband and non-oscillating intraband components of the current. In Fig. 5 the x-direction, J_x and y-direction J_y currents are shown for different field amplitudes, F_0. As one can see, with increasing field amplitude, the magnitudes of both currents increase. The frequency of oscillations of the currents in monolayer h-BN not only depends on the field amplitude, F_0 [Fig. 5] but also depends on the duration of the pulse, τ [Fig. 4].

One of the characteristics of the electric current during the pulse is the transferred electric charge, $\mathbf{Q}$, which is calculated as $\mathbf{Q}_\alpha = \int_{-\infty}^{\infty} \mathbf{J}_\alpha(t)dt$. The transferred charge can also be related to the residual electric polarization of the system. The transferred charge is shown in Fig. 6 as a function of the pulse amplitude for different values of the pulse duration, τ. The longitudinal transferred charge, Q_x, monotonically increases with the field amplitude. Small field amplitudes, up to 0.6 V/Å, transferred charge Q_x has a weak dependence on pulse duration τ, while at large amplitude, it strongly increases with τ. The transverse transferred charge, Q_y, has entirely different depending on both the pulse amplitude and the pulse duration. As a function of the pulse amplitude, F_0, it shows oscillations, which are more pronounced at large values of τ. The transferred charge, Q_y, strongly depends on pulse duration for small and large amplitudes. The results show that the transverse transport is very sensitive to the pulse parameters, such as pulse amplitude and pulse duration. In contrast, the longitudinal transport is more robust to such parameters.

4. Conclusions

In this work, we theoretically predict the fundamentally fastest, ultrafast optical currents that can be induced in monolayer hexagonal Boron Nitride (h-BN) by a circularly-polarized single-oscillation optical pulse. Such a strong pulse redistributes electrons between the bands and generates femtosecond currents during the pulse. The pulse generates both longitudinal and transverse currents. The ultrafast field-driven currents in monolayer hexagonal Boron Nitride are governed by both interband and intraband contribution. As a result, the residual current as a function of time shows oscillations, the frequency of which is determined by the bandgap of the h-BN monolayer. The frequency of oscillations of the currents in monolayer h-BN depends on the field amplitude, F_0 and the duration of the pulse, τ. The CB population distribution is asymmetric with respect to the y-axis both during and after the pulse and the intraband transverse current is none zero.

The longitudinal transferred charge, Q_x, monotonically increases with the field amplitude. Q_x has a weak dependence on the small

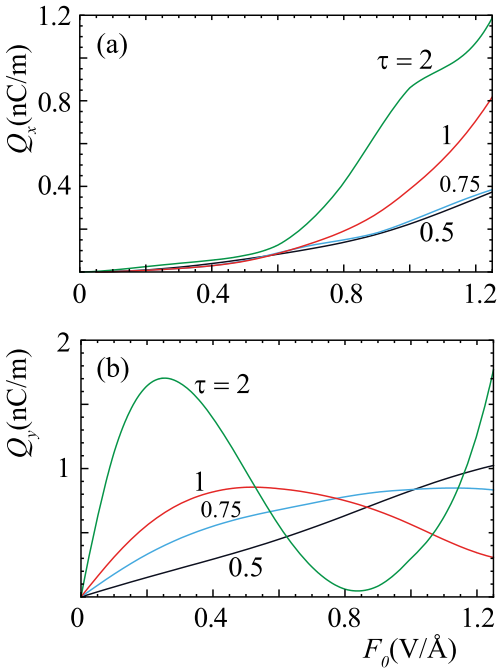

Fig. 6. (Color online) The transferred charge densities are shown as a function of the field amplitude, F_0, for different pulse durations, 0.5 fs, 0.75 fs, 1 fs and 2 fs. (a) The transferred charge density is shown along the direction of the maximum field, Q_x and (b) The transferred charge density is shown in the direction perpendicular to the maximum field, Q_y. The applied optical pulse has right handed circular polarization. The band gap of *h*-BN is 5 eV.

values of τ whereas strong dependence on the large values of τ. The transverse transferred charge, Q_y, has entirely different depending on both the pulse amplitude and the pulse duration. The more pronounced oscillations at large values of τ can be seen as a function of the pulse amplitude, F_0. The transferred charge, Q_y, strongly depends on pulse duration for small and large amplitudes. The results show that the transverse transport is very sensitive to the pulse parameters, such as pulse amplitude and pulse duration. In contrast, the longitudinal transport is more robust to such parameters.

Declaration of competing interest

The authors declare that they have no known competing financial interests or personal relationships that could have appeared to influence the work reported in this paper.

Acknowledgments

Major funding was provided by Grant No. DE-FG02-11ER46789 from the Materials Sciences and Engineering Division of the Office of the Basic Energy Sciences, Office of Science, U.S. Department of Energy. Numerical simulations have been performed using support by Grant No. DE-FG02-01ER15213 from the Chemical Sciences, Biosciences and Geosciences Division, Office of Basic Energy Sciences, Office of Science, US Department of Energy. The work of P.H. was supported by NSF EFRI NewLAW Grant EFMA-17 41691.

References

[1] A. Schiffrin, T. Paasch-Colberg, N. Karpowicz, V. Apalkov, D. Gerster, S. Muhlbrandt, M. Korbman, J. Reichert, M. Schultze, S. Holzner, J.V. Barth, R. Kienberger, R. Ernstorfer, V.S. Yakovlev, M.I. Stockman, F. Krausz, Optical-field-induced current in dielectrics, Nature 493 (7430) (2013) 70–74.

[2] S.A.O. Motlagh, V. Apalkov, M.I. Stockman, Interaction of crystalline topological insulator with an ultrashort laser pulse, Phys. Rev. B 95 (2017) 085438–1–8.

[3] S.A.O. Motlagh, J.S. Wu, V. Apalkov, M.I. Stockman, Fundamentally fastest optical processes at the surface of a topological insulator, Phys. Rev. B 98 (12) (2018) 125410–1–11.

[4] F. Nematollahi, S.A.O. Motlagh, V. Apalkov, M.I. Stockman, Weyl semimetals in ultrafast laser fields, Phys. Rev. B 99 (24) (2019) 245409–1–9.

[5] C. Heide, T. Higuchi, H.B. Weber, P. Hommelhoff, Coherent electron trajectory control in graphene, Phys. Rev. Lett. 121 (2018) 207401–1–5.

[6] H.Z. Liu, Y.L. Li, Y.S. You, S. Ghimire, T.F. Heinz, D.A. Reis, High-harmonic generation from an atomically thin semiconductor, Nat. Phys. 13 (2017) 262–266.

[7] A. Kaiser, B. Rethfeld, M. Vicanek, G. Simon, Microscopic processes in dielectrics under irradiation by subpicosecond laser pulses, Phys. Rev. B 61 (2000) 11437–11450.

[8] C. Heide, T. Boolakee, T. Higuchi, H.B. Weber, P. Hommelhoff, Interaction of carrier envelope phase-stable laser pulses with graphene: the transition from the weak-field to the strong-field regime, New J. Phys. 21 (2019) 045003.

[9] E. Gruber, R.A. Wilhelm, R. Pétuya, V. Smejkal, R. Kozubek, A. Hierzenberger, B.C. Bayer, I. Aldazabal, A.K. Kazansky, F. Libisch, A.V. Krasheninnikov, M. Schleberger, S. Facsko, A.G. Borisov, A. Arnau, F. Aumayr, Ultrafast electronic response of graphene to a strong and localized electric field, Nature Commun. 7 (2016) 13948.

[10] T. Higuchi, C. Heide, K. Ullmann, H.B. Weber, P. Hommelhoff, Light-field-driven currents in graphene, Nature 550 (7675) (2017) 224–228.

[11] M. Trushin, A. Grupp, G. Soavi, A. Budweg, D.D. Fazio, U. Sassi, A. Lombardo, A.C. Ferrari, W. Belzig, A. Leitenstorfer, D. Brida, Ultrafast pseudospin dynamics in graphene, Phys. Rev. B 92 (2015) 165429.

[12] M.S. Wismer, M.I. Stockman, V.S. Yakovlev, Ultrafast optical faraday effect in transparent solids, Phys. Rev. B 96 (2017) 224301.

[13] D. Sun, J.W. Lai, J.C. Ma, Q.S. Wang, J. Liu, Review of ultrafast spectroscopy studies of valley carrier dynamics in two-dimensional semiconducting transition metal dichalcogenides, Chin. Phys. B 26 (3) (2017).

[14] X. Xu, W. Zhang, J. Wang, L. Zhang, Topological chiral phonons in center-stacked bilayer triangle lattices, J. Phys.: Condens. Matter 30 (22) (2018) 225401.

[15] S.A.O. Motlagh, F. Nematollahi, A. Mitra, A.J. Zafar, V. Apalkov, M.I. Stockman, Ultrafast optical currents in gapped graphene, J. Phys.: Condens. Matter 32 (6) (2020) 065305.

[16] S.A. Oliaei Motlagh, F. Nematollahi, V. Apalkov, M.I. Stockman, Topological resonance and single-optical-cycle valley polarization in gapped graphene, Phys. Rev. B 100 (2019) 115431.

[17] S.Z. Butler, S.M. Hollen, L.Y. Cao, Y. Cui, J.A. Gupta, H.R. Gutierrez, T.F. Heinz, S.S. Hong, J.X. Huang, A.F. Ismach, E. Johnston-Halperin, M. Kuno, V.V. Plashnitsa, R.D. Robinson, R.S. Ruoff, S. Salahuddin, J. Shan, L. Shi, M.G. Spencer, M. Terrones, W. Windl, J.E. Goldberger, Progress, challenges, and opportunities in two-dimensional materials beyond graphene, Acs Nano 7 (4) (2013) 2898–2926.

[18] D. Teweldebrhan, V. Goyal, A.A. Balandin, Exfoliation and characterization of bismuth telluride atomic quintuples and quasi-two-dimensional crystals, Nano Lett. 10 (4) (2010) 1209–1218.

[19] K. Endo, K. Komatsu, T. Iwasaki, E. Watanabe, D. Tsuya, K. Watanabe, T. Taniguchi, Y. Noguchi, Y. Wakayama, Y. Morita, S. Moriyama, Topological valley currents in bilayer graphene/hexagonal boron nitride superlattices, Appl. Phys. Lett. 114 (24) (2019) 243105.

[20] K.S. Novoselov, D. Jiang, F. Schedin, T.J. Booth, V.V. Khotkevich, S.V. Morozov, A.K. Geim, Two-dimensional atomic crystals, 102 (30), 2005, pp. 10451–10453.

[21] D. Golberg, Y. Bando, Y. Huang, T. Terao, M. Mitome, C. Tang, C. Zhi, Boron nitride nanotubes and nanosheets, ACS Nano 4 (6) (2010) 2979–2993.

[22] C. Elias, P. Valvin, T.o. Pelini, Direct band-gap crossover in epitaxial monolayer boron nitrides, Nature Commun. 10 (6) (2019) 2639–2649.

[23] C.E. Ekuma, V. Dobrosavljev, D. Gunlycke, First-principles-based method for electron localization: Application to monolayer hexagonal boron nitride, Phys. Rev. Lett. 118 (2017) 106404.

[24] S. Saha, D. Muthu, D. Golberg, C. Tang, C. Zhi, Y. Bando, A. Sood, Comparative high pressure Raman study of boron nitride nanotubes and hexagonal boron nitride, Chem. Phys. Lett. 421 (1) (2006) 86–90.

[25] S. Saha, D. Muthu, D. Golberg, C. Tang, C. Zhi, Y. Bando, A. Sood, Energy bands and optical properties of hexagonal boron nitride and graphite, Nuovo Cimento B 64 (1969) 117–144.

[26] S.A.O. Motlagh, J.-S. Wu, V. Apalkov, M.I. Stockman, Femtosecond valley polarization and topological resonances in transition metal dichalcogenides, Phys. Rev. B 98 (2018) 081406(R)–1–6.

[27] P. Hewageegana, Interaction of ultrafast optical pulse with monolayer hexagonal boron nitride (h-BN), Physica E 134 (2021) 114906.

[28] S.A. Oliaei Motlagh, V. Apalkov, M.I. Stockman, Transition metal dichalcogenide monolayers in an ultrashort optical pulse: Femtosecond currents and anisotropic electron dynamics, Phys. Rev. B 103 (2021) 155416.

[29] D. Xiao, G.B. Liu, W.X. Feng, X.D. Xu, W. Yao, Coupled spin and valley physics in monolayers of MoS_2 and other group-VI dichalcogenides, Phys. Rev. Lett. 108 (19) (2012).

[30] H.L. Zeng, J.F. Dai, W. Yao, D. Xiao, X.D. Cui, Valley polarization in MoS_2 monolayers by optical pumping, Nature Nanotechnol. 7 (8) (2012) 490–493.

[31] K.F. Mak, K.L. He, J. Shan, T.F. Heinz, Control of valley polarization in monolayer MoS_2 by optical helicity, Nature Nanotechnol. 7 (2012) 494–498.
[32] T. Cao, G. Wang, W.P. Han, H.Q. Ye, C.R. Zhu, J.R. Shi, Q. Niu, P.H. Tan, E. Wang, B.L. Liu, J. Feng, Valley-selective circular dichroism of monolayer molybdenum disulphide, Nature Commun. 3 (2012) 887–1–5.
[33] A.M. Jones, H.Y. Yu, N.J. Ghimire, S.F. Wu, G. Aivazian, J.S. Ross, B. Zhao, J.Q. Yan, D.G. Mandrus, D. Xiao, W. Yao, X.D. Xu, Optical generation of excitonic valley coherence in monolayer WSe_2, Nature Nanotechnol. 8 (9) (2013) 634–638.
[34] E.J. Sie, J. McIver, Y.H. Lee, L. Fu, J. Kong, N. Gedik, Valley-selective optical Stark effect in monolayer WS_2, Nature Mater. 14 (3) (2015) 290–294.
[35] Y. Shi, N. Gillgren, T. Espiritu, S. Tran, J. Yang, K. Watanabe, T. Taniguchi, C.N. Lau, Weak localization and electron–electron interactions in few layer black phosphorus devices, 2D Mater. 3 (3) (2016) 034003.
[36] F. Bloch, Über die Quantenmechanik der Elektronen in Kristallgittern, Z. Phys. A 52 (1929) 555–600.
[37] W.V. Houston, Acceleration of electrons in a crystal lattice, Phys. Rev. 57 (1940) 184–186.
[38] W.V. Houston, Acceleration of electrons in a crystal lattice, Phys. Rev. 57 (1940) 184–186.
[39] F. Wilczek, A. Zee, Appearance of gauge structure in simple dynamical systems, Phys. Rev. Lett. 52 (1984) 2111–2114.
[40] D. Xiao, M.-C. Chang, Q. Niu, Berry phase effects on electronic properties, Rev. Modern Phys. 82 (2010) 1959–2007.
[41] F. Yang, R.B. Liu, Nonlinear optical response induced by non-Abelian Berry curvature in time-reversal-invariant insulators, Phys. Rev. B 90 (2014) 245205.
[42] P.B. Corkum, F. Krausz, Attosecond science, Nat. Phys. 3 (2007) 381–387.
[43] F. Krausz, M. Ivanov, Attosecond physics, Rev. Modern Phys. 81 (2009) 163–234.
[44] F. Krausz, M.I. Stockman, Attosecond metrology: from electron capture to future signal processing, Nature Photon. 8 (3) (2014) 205–213.
[45] H. Koochaki Kelardeh, V. Apalkov, M.I. Stockman, Graphene superlattices in strong circularly polarized fields: Chirality, berry phase, and attosecond dynamics, Phys. Rev. B 96 (2017) 075409.